

Supporting Information

Manganese(II) Phosphate Nanosheet Assembly with Native Out-of-Plane Mn Centres for Electrocatalytic Water Oxidation

Hongfei Liu,^{#a} Xueqing Gao,^{#a} Xiaolong Yao,^{#b} Mingxing Chen,^c Guojun Zhou,^a Jing Qi,^a Xueli Zhao,^a Weichao Wang,^{*b} Wei Zhang,^{*a} and Rui Cao^{*ac}

^aKey Laboratory of Applied Surface and Colloid Chemistry, Ministry of Education and School of Chemistry and Chemical Engineering, Shaanxi Normal University, Xi'an 710119, China

^bDepartment of Electronics, Nankai University, Tianjin 300071, China

^cDepartment of Chemistry, Renmin University of China, Beijing 100872, China

[#]These authors contributed equally to this work

*Correspondence to: zw@snnu.edu.cn; ruiicao@ruc.edu.cn; weichaowang@nankai.edu.cn

General materials

Manganese(II) chloride (MnCl_2 , 99%, Energy Chemical), phosphoric acid ($\geq 85\%$, Xilong Chemical Co.), ethylenediamine ($\geq 99\%$, Tianli Chemical Co.), D_2O ($> 99.8\%$, Beijing Chongxi), MnO (99%, Aladdin Reagent), $\text{NaH}_2\text{PO}_4 \cdot 2\text{H}_2\text{O}$ (99.99%, Heowns Biochem LLC) and Na_2HPO_4 (99.99%, Energy Chemical) were obtained from commercial suppliers and used without further purification unless otherwise noted. Milli-Q water of $18 \text{ M}\Omega\cdot\text{cm}$ was used in all experiments.

Material synthesis

Synthesis of ethylene-diammonium manganese phosphate layered nanoplates (Mn-LNPs). In a typical synthesis of the Mn-LNPs, an aqueous solution containing 45 mL of water, 5 mmol of MnCl_2 and 72 mmol of H_3PO_4 was stirred at room temperature until the solution is clear and transparent. Ethylenediamine was added into the mixture dropwise to control the pH of the solution at 5. Then, the obtained suspension was sealed in a 100 mL Teflon-lined stainless steel autoclave and heated at 165°C for 15 h. After the mixture was air-cooled to room temperature, white products were collected and washed thoroughly by centrifugation with water. The obtained white solids were subjected to further process for the preparation of manganese(II) phosphate nanosheet assembly (MnPi) without drying. For physical characterizations, the solids were dried in an electric oven at 60°C in air. Noteworthily, ethylenediamine was used as the intercalation reagent, and the pH of the solution should be controlled strictly in this system. Parallel tests were conducted by varying the reaction conditions including the hydrothermal temperature, ethylenediamine concentration (pH), and reaction time. The pH of the reaction solution was controlled by ethylenediamine. Different morphologies can be obtained with different pHs, as shown in Figure S1.

Synthesis of manganese(II) phosphate nanosheet assembly (MnPi) electrocatalyst. The MnPi electrocatalyst was obtained by the method of liquid-phase ultrasound transformation of the Mn-LNPs. In a typical experiment, about 100 mg of Mn-LNPs were dispersed in a capped reagent bottle with 250 mL of water. Then, the mixture was sonicated for 4 h ceaselessly to form the MnPi. The obtained product was collected from natural sedimentation and dried in an electric oven at 60°C . Generally, a reasonable choice of liquid media, sonication time and concentration is pivotal for the morphology of the derived nanosheets. Parallel tests were conducted by varying the conditions of the liquid media, sonication time and concentration. N-methylpyrrolidinone (NMP), N,N-dimethylformamide (DMF), absolute ethyl alcohol (EtOH) and Milli-Q water were surveyed to choose the optimal liquid media. Relevant results are shown in Figure S2-S4.

Characterization

Scanning electron microscopy (SEM) images were collected on a Hitachi SU8020 cold-emission field emission scanning electron microscope (FESEM). Transmission electron microscopy (TEM) and high-angle annular dark field (HAADF) scanning TEM images were obtained on a JEOL JEM-2100 TEM. Energy dispersive X-ray analysis (EDX) was carried out on an AMETEK Materials Analysis. An x-ray diffractometer (Rigaku D/Max2550VB+/PC) was used to record the X-ray diffraction (XRD) patterns. X-ray photoelectron spectroscopy (XPS) analyses of the samples were performed on a Kratos AXIS ULTRA XPS analyzer with monochromatized $\text{Al K}\alpha$ ($h\nu = 1486.6 \text{ eV}$) X-ray source. The XPS binding

energies were corrected using C1s peak of adventitious carbon at 284.6 eV. Atomic force microscope (AFM) images were obtained from a Bronk Dimension ICON AFM. Thermo gravimetric analysis (TGA) was carried out with a temperature ramp of 5 °C/min under N₂ flow at 100 mL/min over 25°C to 800 °C in a TA Instruments SDT Q600. The C and N contents of materials were determined by a Vario EL III CHNS/O Elemental Analyzer. Magnetic measurements were performed with powders on a Quantum Design MPMS-XL7 SQUID, and the data were corrected for the diamagnetic contribution calculated with Pascal constants. The Mn:P molar ratio of the MnPi sample before and after electrolysis was determined by Perkin Elmer Optima 5300DV inductively coupled plasma-optical emission spectrometry (ICP-OES). The samples are dissolved in nitric acid for the ICP-OES analysis.

Electrochemical studies

All electrochemical tests were performed on a CHI 660E electrochemical workstation at room temperature with a standard three-electrode setup. An aqueous sodium phosphate buffer (0.05 M, pH = 7) was used as the electrolyte. Saturated Ag/AgCl and Pt wire were used as the reference and auxiliary electrode, respectively. The working electrode was prepared by a drop-casting method. In a typical experiment, 4 mg of the as-prepared catalyst was dispersed into 1 mL of water-ethanol (volume ratio of 2:1) with 30 µL of Nafion solution (5 wt%, DuPont). A homogeneous ink was formed via sonicating the obtained mixture. Subsequently, 5 µL of the ink was drop-casted evenly onto a polished glassy carbon electrode (the geometric surface area is 0.07 cm²) and was dried naturally. Cyclic voltammograms (CVs) were performed at a potential scan rate of 50 mV s⁻¹ with iR-compensation. In these measurements, the working electrode was CV scanned several times in order to get a steady response before data recording. Current densities were presented by geometric surface areas. Controlled potential electrolysis (CPE) was used to evaluate the stability of the catalyst without iR-compensation. Tafel plots were obtained from stable state currents at different potentials.

Computational studies

The first-principles density functional theory (DFT) calculations are performed with GGA+U functional using the PWmat code, which runs on graphics processing unit (GPU) processors.^[1] NCPP-SG15-PBE pseudopotentials are used in the calculations.^[2] The effective U parameter of 4.0 eV is used for Mn d orbitals.^[3] The cutoff energy for plane-wave basis set is consistently chosen to be 50 Ryd, and the k-space is sampled by a 4×2×2 Monkhorst-Pack k-point mesh.^[4] The lattice constants of metaswitzerite Mn₃(PO₄)₂•4H₂O are fixed at the experimental values of 8.50 Å, 13.17 Å and 17.21 Å.^[5] Atomic positions are relaxed until the forces are reduced below 0.02 eV/Å.

Equation S1:

$$\left(\frac{\partial E}{\partial \text{pH}}\right)_j = -\left(\frac{\partial E}{\partial \log(j)}\right)_{\text{pH}} \left(\frac{\partial \log(j)}{\partial \text{pH}}\right)_E \quad (1)$$

Table S1 The CHNS elemental analysis of the investigated samples.

samples	Contents (wt%)			
	N /%	C /%	H /%	S /%
Mn-LNPs	5.91	4.12	2.31	0.401
	5.90	4.23	2.82	0.953
	5.89	4.22	2.75	0.886
MnPi before electrolysis	0.080	0.022	0.732	0.377
	0.099	0.024	0.605	0.410
	0.094	0.025	0.654	0.377
MnPi after electrolysis	0.085	0.106	0.620	0.403
	0.087	0.164	0.556	0.355
	0.079	0.193	0.505	0.347

Table S2 The comparison of electrocatalytic OER performance of Mn-based materials in near neutral solutions.

Catalysts	Substrates	Electrolytes	Overpotential (@ 1.0 mA/cm ²)	Reference
MnPi	GC	pH = 7, 0.05 M PBS	563 mV	This work
δ -MnO ₂	FTO	pH = 6, 0.5 M Na ₂ SO ₄	724 mV	<i>J. Am. Chem. Soc.</i> 2012, 134 , 1519
MnO ₂	FTO	pH = 8, 0.5 M Na ₂ SO ₄	0.03 mA/cm ² (at η = 600 mV)	<i>J. Am. Chem. Soc.</i> 2012, 134 , 18153
MnCat	ITO	pH = 7, 0.1 M PBS	593 mV	<i>Energy Environ. Sci.</i> 2012, 5 , 7081
MnOx	ITO	pH = 7, 0.1 M PBS	623 mV	<i>Angew. Chem. Int. Ed.</i> 2013, 52 , 13206
s-MnOx	GC	pH = 7, 0.1 M PBS	470 mV	<i>Energy Environ. Sci.</i> , 2013, 6 , 2745
i-MnOx			0.36 mA/cm ² (at η = 470 mV)	
Mn ₃ (PO ₄) ₂	FTO	pH = 7, 0.5 M PBS	0.316 mA/cm ² (at η = 680 mV)	<i>J. Am. Chem. Soc.</i> 2014, 136 , 7435
LiMnP ₂ O ₇	FTO	pH = 7, 0.5 M PBS	0.5 mA/cm ² (at η = 680 mV)	<i>J. Am. Chem. Soc.</i> 2014, 136 , 4201
Mn ₅ O ₈	FTO	pH = 7.8, 0.3 M PBS	550 mV	<i>ACS Catal.</i> 2015, 5 , 4624
MnOx	FTO	pH = 7.0, 1.0 M PBS	330 mV	<i>ACS Catal.</i> 2017, 7 , 6311
MnO-70 nm	FTO	pH = 7, 0.5 M PBS	503	<i>J. Am. Chem. Soc.</i> 2017, 139 , 2277
MnO-150 nm			463	
MnO-300 nm			433	
MnO-600 nm			433	
NOTE: Some of these studies focus on the detailed mechanism studies rather than an optimization of OER activity.				

Table S3 The Mn:P molar ratio in the MnPi sample before and after electrolysis determined by ICP-OES. Two parallel tests were performed for each sample.

samples	MnPi-1	MnPi-2	MnPi after CPE-1	MnPi after CPE-2
Mn/P molar ratio	1.433	1.443	1.460	1.438

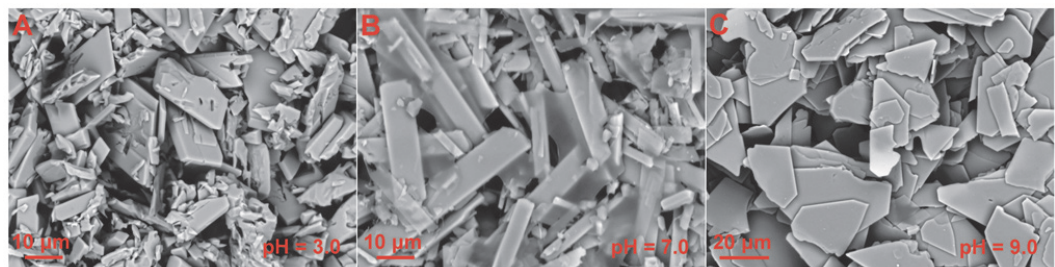


Fig. S1 The SEM images of bulk manganese phosphates synthesized in solutions with different pH values.

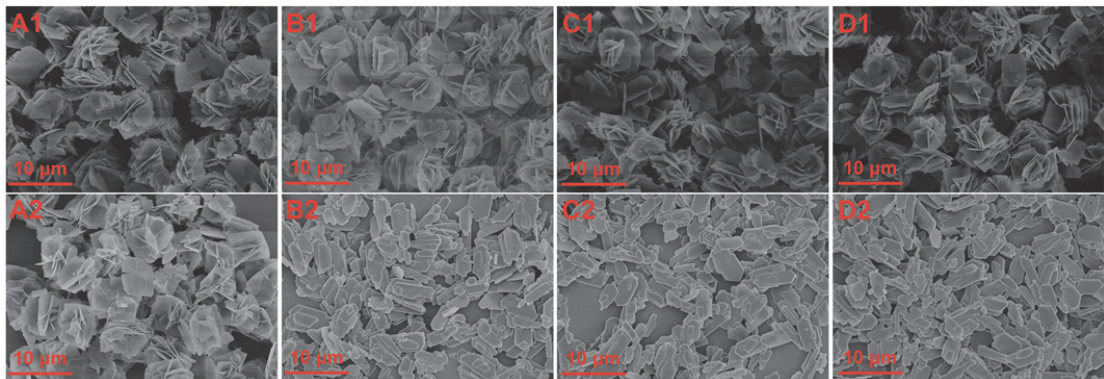


Fig. S2 (A1-D1) The SEM images of the sonication-derived nanosheet assembly in different liquid media. **(A2-D2)** The SEM images of the corresponding materials after being kept for one week for equilibrium in the liquid media. **A:** H₂O; **B:** DMF; **C:** NMP; **D:** EtOH.

Generally, a reasonable choice of the liquid media, sonication time and concentration of bulk material is pivotal to generate uniform assembly. A successful liquid-phase ultrasound transformation requires the following two fulfillments. First, the interlayer interaction between the adjacent layers should be broken through the removal of the intercalated molecules by offering energy and solvent molecules. Second, the resulting nanosheets should be prevented against aggregation by appropriate equilibrium between the solids and the liquid media. In our system, pure water appeared to be the optimized liquid media, as compared with other traditional organic solvents. Aggregation of the nanosheets occurs in N-methylpyrrolidinone (NMP), N,N-dimethylformamide (DMF) and absolute ethanol (EtOH) after a week. However, the sonication-derived nanosheet assembly is stabilized against aggregation in water. The stabilization of the nanosheets can be realized when equilibrium between the nanosheets and solvent are well maintained. Such equilibrium is associated with the surface tension, Hildebrand parameters and Hansen parameters.

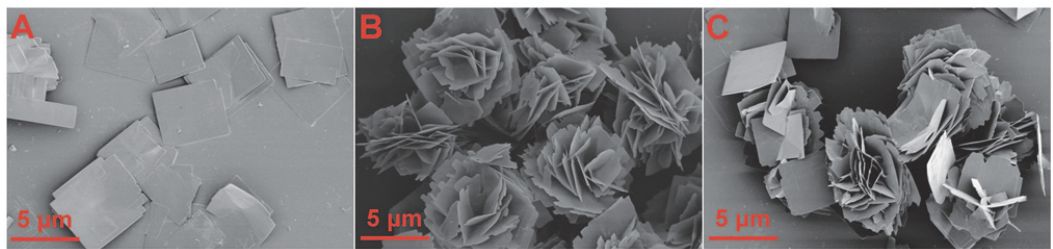


Fig. S3 The SEM images of the nanosheets prepared from sonication in water with different starting concentration of the bulk nanoplates (Mn-LNPs). **A:** 50 mg of Mn-LNPs in 250 mL of water; **B:** 100 mg of Mn-LNPs in 250 mL of water; **C:** 200 mg of Mn-LNPs in 250 mL of water.

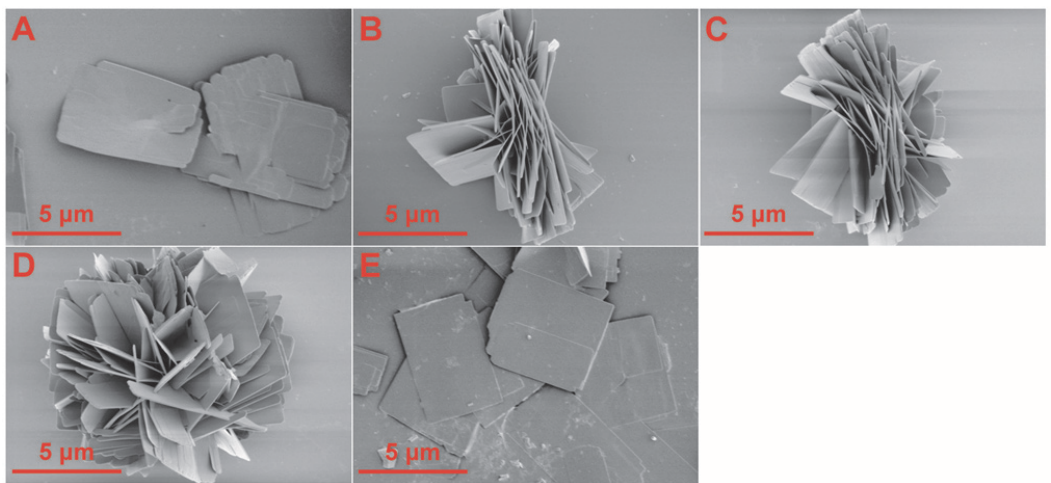


Fig. S4 The SEM images of the nanosheets prepared in water with different sonication time. **A:** 0.5 h; **B:** 1 h; **C:** 2 h; **D:** 4 h; **E:** 8 h.

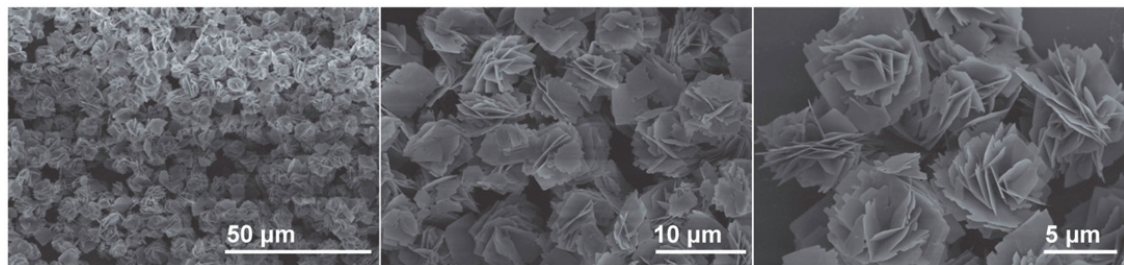


Fig. S5 The SEM images of the nanosheet assembly with different magnifications. Sonication conditions: 100 mg of Mn-LNPs in 250 mL of water, 4 h.

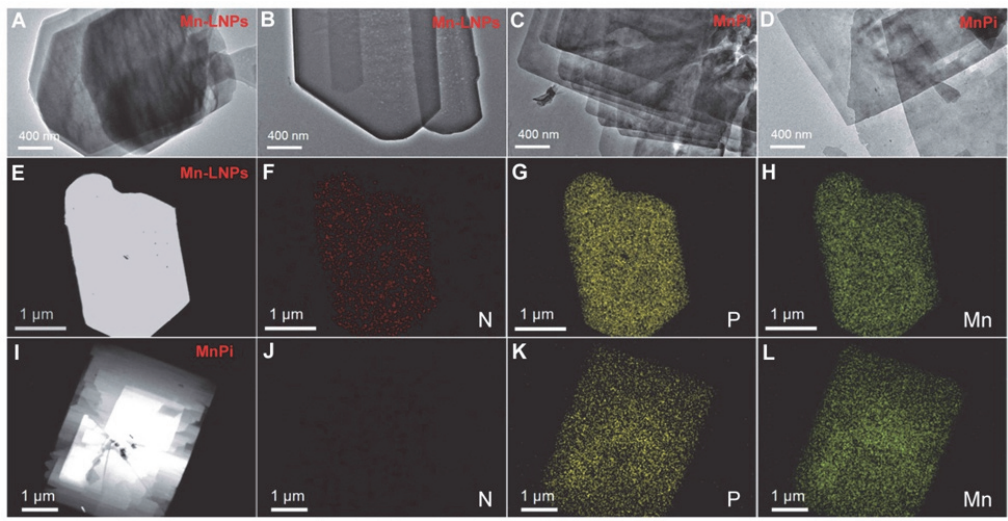


Fig. S6 The TEM images of the Mn-LNPs (**A**, **B**) and MnPi (**C**, **D**). The HAADF STEM images and the corresponding EDX elemental mapping images of Mn-LNPs (**E-H**) and MnPi (**I-L**).

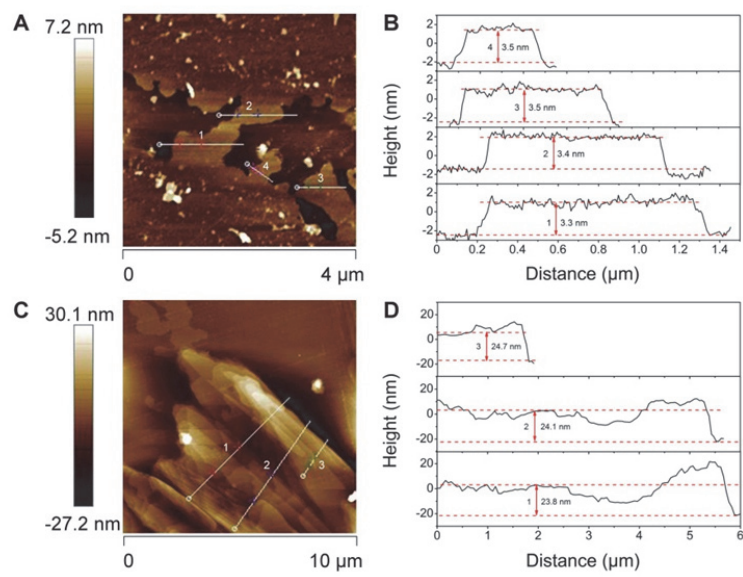


Fig. S7 The AFM images and the corresponding height plots of the MnPi (**A, B**) and Mn-LNPs (**C, D**).

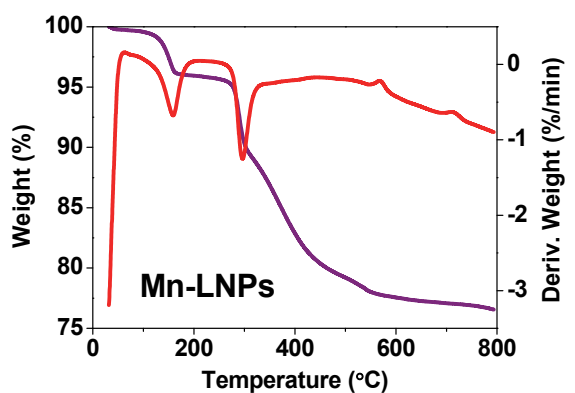


Fig. S8 The thermal gravimetric analysis (TGA) and derivative thermogravimetric (DTG) analysis studies of the Mn-LNPs. The first loss is from the lattice water, and the anionic sheets decompose at higher temperatures.^[6]

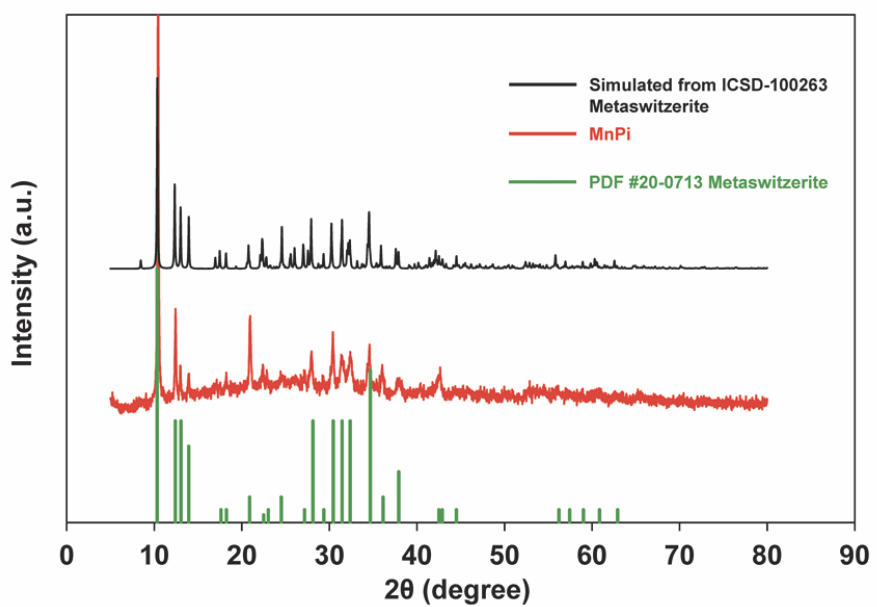


Fig. S9 The XRD patterns of the metaswitzerite (PDF #20-0713), the as-prepared MnPi and simulated XRD patterns from crystal structure data of metaswitzerite (ICSD-100263).

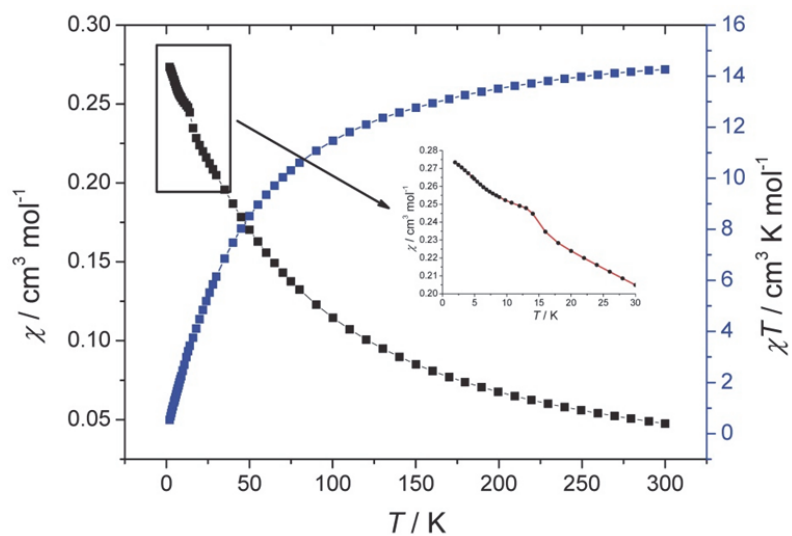


Fig. S10 The temperature dependences of magnetic susceptibility of MnPi. The inset represents enlarged low temperature magnetic susceptibility. The result resemble that of Mn(II) phosphate with high-spin state of Mn(II) ($S = 5/2$).^[7]

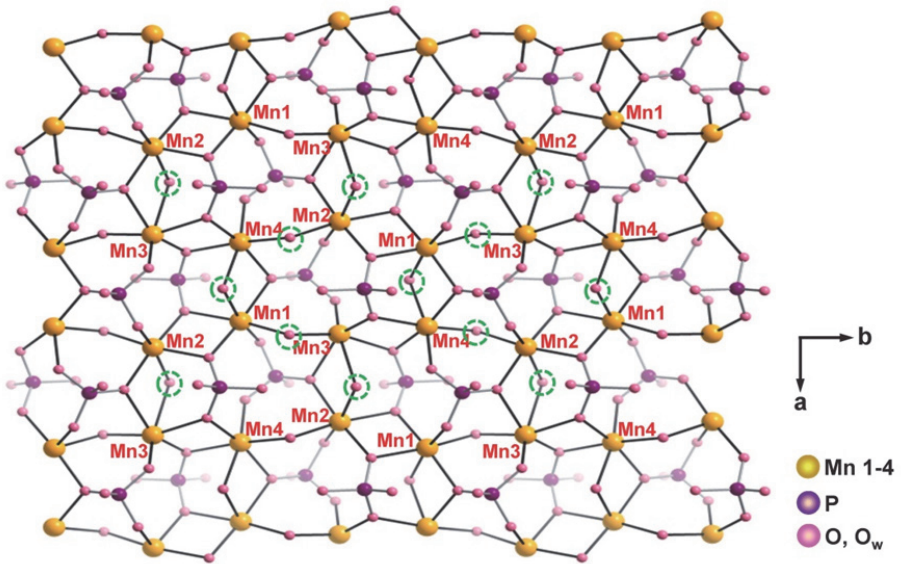


Fig. S11 The crystal structure of the Mn1-4 layer parallel to the (001) plane. In the center area, the Mn atoms are marked and the $\mu_2\text{-O}_w$ atoms from water are labeled with green circles. O_w : oxygen from water. In detail, Mn(1) is surrounded by Mn(2) (O-O edge sharing), Mn(3) (O_w corner sharing) and Mn(4) (O-O_w edge sharing). Mn(2) is surrounded by Mn(1) (O-O edge sharing), Mn(3) (O-O_w edge sharing) and Mn(4) (O_w corner sharing). Mn(3) is surrounded by Mn(1) (O_w corner sharing), Mn(2) (O-O_w edge sharing) and Mn(4) (O-O edge sharing). Mn(4) is surrounded by Mn(1) (O-O_w edge sharing), Mn(2) (O_w corner sharing) and Mn(3) (O-O edge sharing).

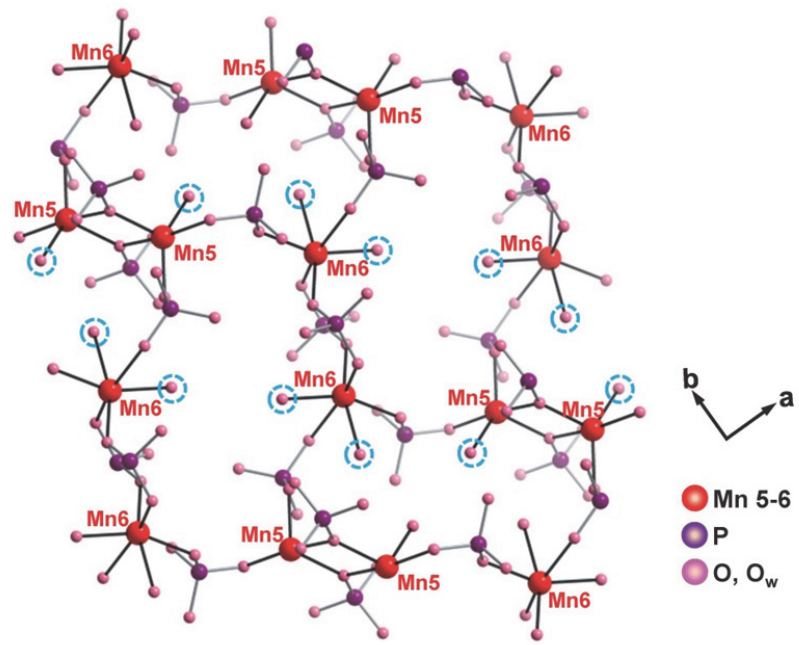


Fig. S12 The crystal structure of the Mn5-6 as out-of-plane sites of the Mn1-4 layer. The Mn atoms are marked and the terminal O_w atoms from water are labeled with blue circles. O_w: oxygen from water. In detail, Mn(5) is connected to another Mn(5) via O-O edge sharing and to Mn(2) in a parallel layer via O corner sharing. Mn(6) is connected to Mn(1) in a parallel layer via O corner sharing.

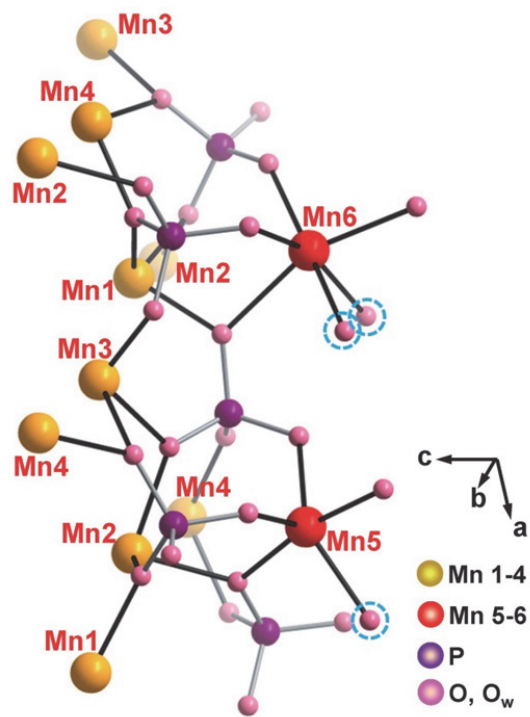


Fig. S13 The crystal structure of the connection between the Mn1-4 layer and the out-of-plane Mn5-6. The Mn atoms are marked and the terminal O_w atoms from water are labeled with blue circles. O_w : oxygen from water.

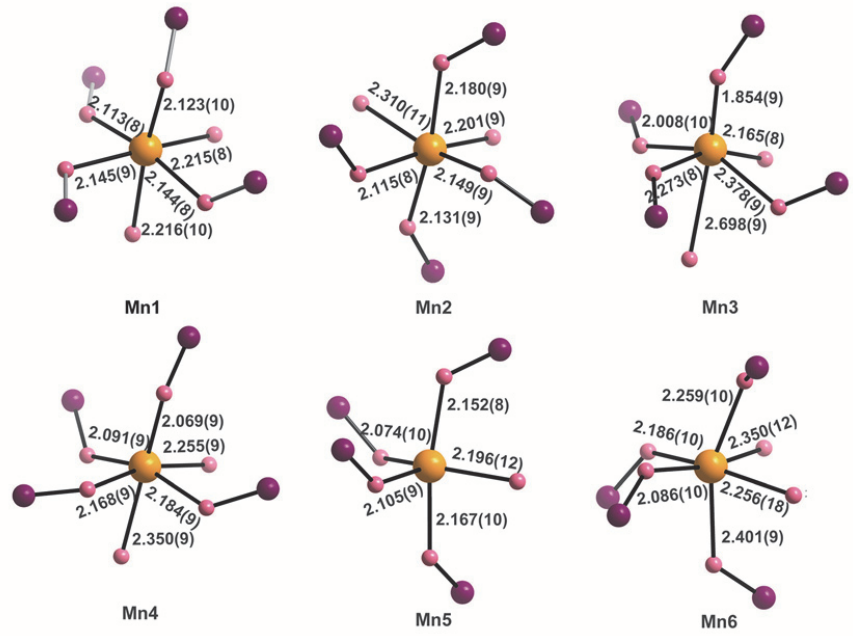


Fig. S14 The coordination geometry of the six different Mn sites with Mn-O bond lengths. The oxygen atoms that are not connected to P are from water.

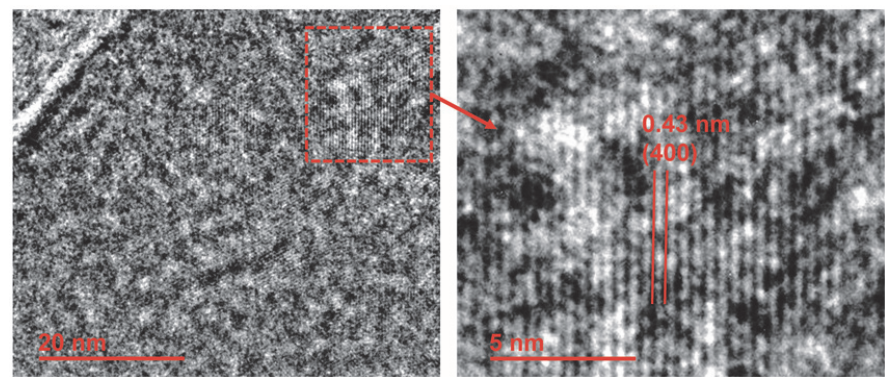


Fig. S15 The HRTEM image of the basal plane of the nanosheet of MnPi. The lattice spacing at 0.43 nm indicates the layers are stacked perpendicular to the *c*-axis in the nanosheet structure.

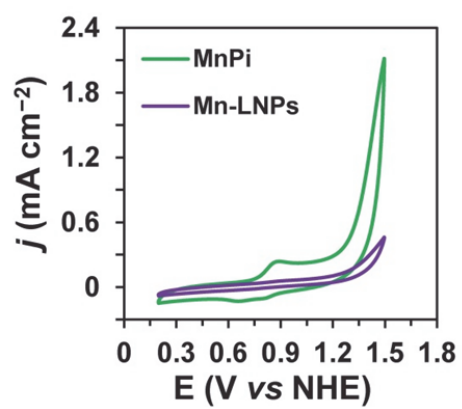


Fig. S16 The CV curves of the MnPi and Mn-LNPs samples in a 0.05 M phosphate buffer solution (pH = 7.0) on a glassy carbon electrode.

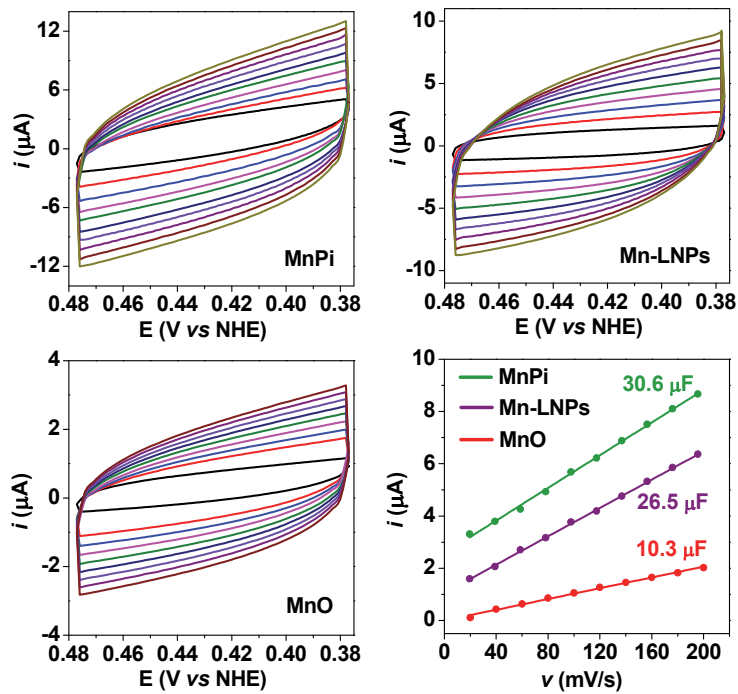


Fig. S17 The charging currents of MnPi, Mn-LNPs and MnO recorded in the non-Faradaic potential region at different scan rates. The anodic charging current at 0.425 V plotted against the scan rates, the slope of which is the capacitance that is proportional to the electrochemical surface areas (ECSA).

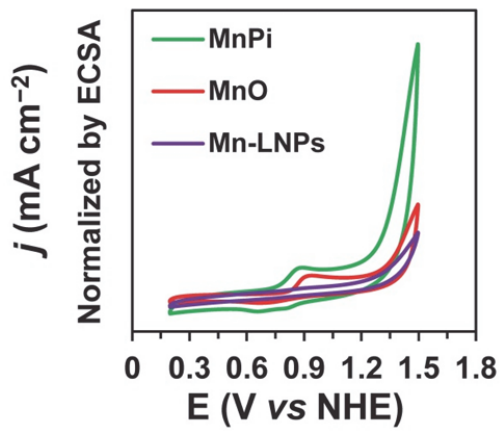


Fig. S18 The normalized OER activity comparison of MnPi, Mn-LNPs and MnO. The original activity is normalized by the capacitances of the materials determined in Fig. S17.

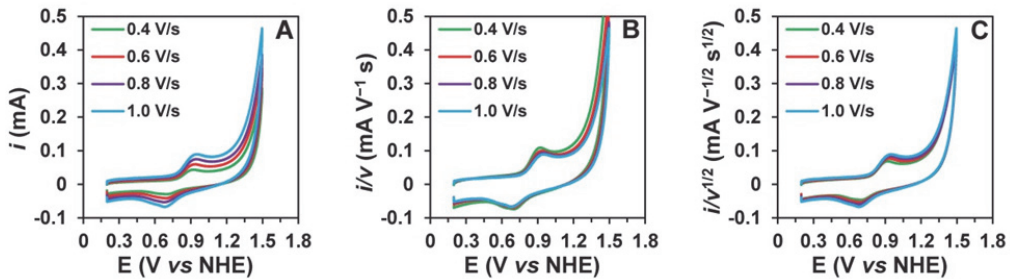


Fig. S19 The CV current-potential responses of i , i/v , and $i/v^{1/2}$ of the MnPi electrocatalyst at different scan rates in a 0.05 M phosphate buffer solution ($\text{pH} = 7.0$). The linear relationship in these responses indicates the kinetic control by catalytic reaction, double-layer capacitive currents and diffusion, respectively.

The following information can be concluded. First, the quasi-reversible $\text{Mn}^{\text{II}/\text{III}}$ redox couple becomes reversible at high scan rates (Figure S19A), indicating that the resting states can be fully regenerated after the completion of the catalytic cycle and the resting states are sensitive to its surroundings (electrolyte, oxygen, etc.). Second, the material displays a semiconductor behavior within the complete precatalytic potential range, which is consistent with the nature of transition metal phosphates. Third, the currents before the first oxidation ($i \propto v$ region, Figure S19B) are kinetic-controlled by double-layer capacitance ($\sim 30.9 \mu\text{F}$). After that, the currents are generally kinetic-controlled by diffusion ($i \propto \sqrt{v}$ region, Figure S19C), indicating that there is still room for increasing the structure voids in the layered MnPi toward higher performance.

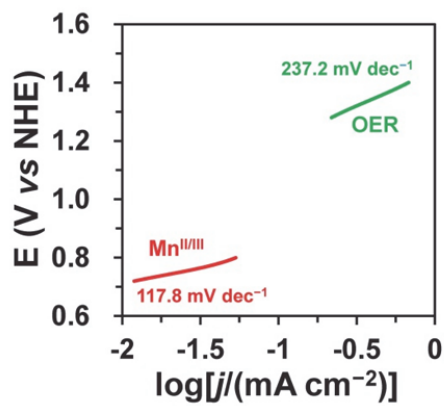


Fig. S20 The Tafel plots of the MnPi sample at the Tafel region of the $Mn^{II/III}$ oxidation (red) and electrocatalytic OER (green).

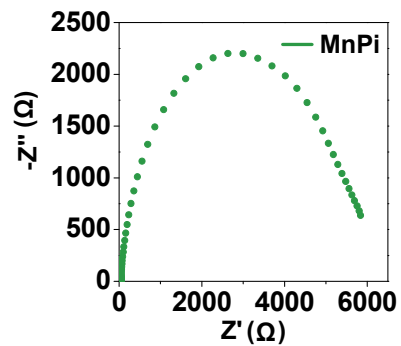


Fig. S21 The Nyquist plot of MnPi derived from the electrochemical impedance spectroscopy at 1.5 V vs NHE in an aqueous phosphate buffer (0.05 M, pH = 7).

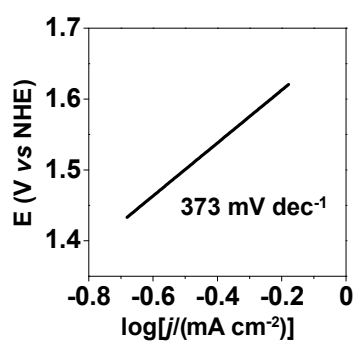


Fig. S22 The Tafel plot of the MnPi sample in a unbuffered 0.05 M NaClO₄ solution.

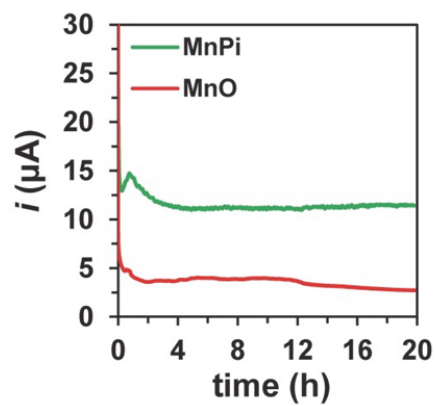


Fig. S23 The controlled potential electrolysis of the MnPi and MnO samples on GC electrode in a 0.05 M phosphate buffer solution (pH = 7.0).

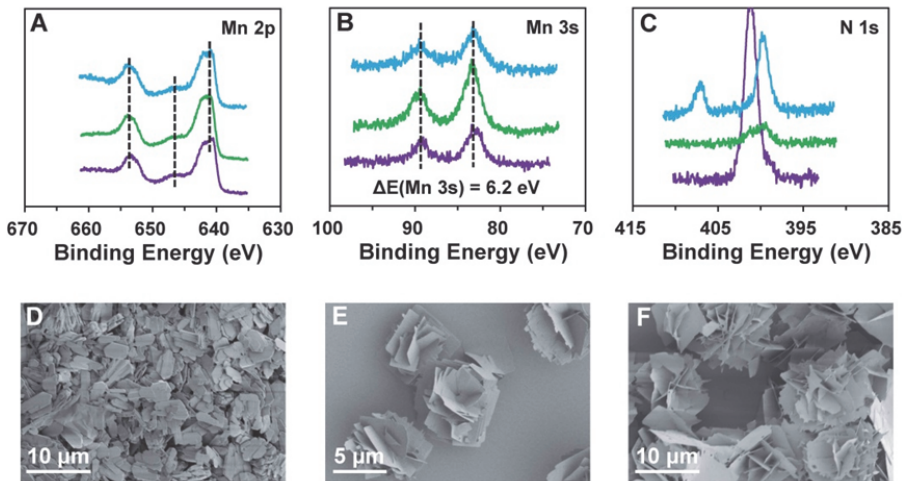


Fig. S24 (A-C) The XPS spectra of the Mn-LNPs (purple lines), MnPi (green lines) and MnPi after electrolysis (blue lines). The SEM images of the Mn-LNPs (D), MnPi (E) and MnPi after electrolysis (F).

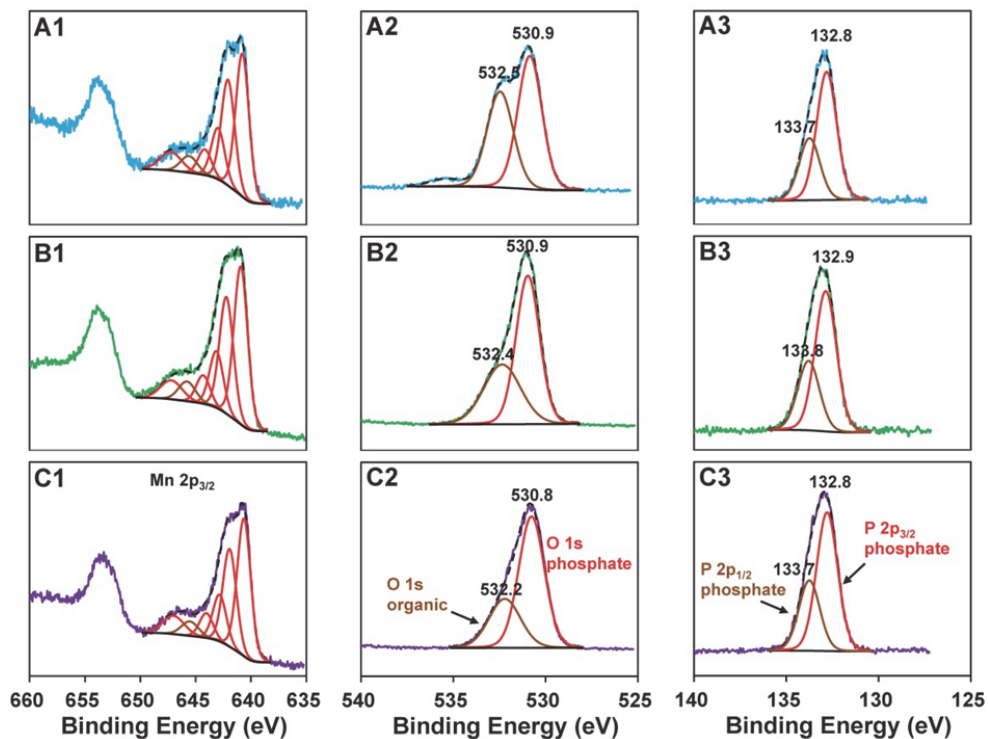


Fig. S25 The XPS spectra of the Mn-LNPs (C1-C3), MnPi (B1-B3) and MnPi after electrolysis (A1-A3) near the binding energies of Mn 2p (A1, B1 and C1), O 1s (A2, B2 and C2) and P 2p (A3, B3 and C3).

The peak positions of the Mn spectra remained almost unchanged, indicating the structure stability of Mn coordination after sonication and electrolysis. The Mn 2p_{3/2} peaks are fitted according to the protocols established by Nesbitt and Banerjee,^[8] displaying Mn(II) multiplets (red lines) and satellites (brown lines).

The main peak position of the Mn 2p_{3/2} (641-642 eV), the presence of the shake-up peak of Mn 2p_{3/2} (~647 eV), and the peak splitting of the Mn 3s spectra at ~6.2 eV all demonstrate the valence of Mn in the materials is two.^[9] Of particular note is that the N 1s spectra of these three samples changed obviously. The strong N 1s signal of the Mn-LNPs (~401 eV) is from the intercalated EDA. This peak is significantly reduced after the sonication treatment, as shown in the N 1s spectrum of the MnPi. After electrolysis, two new N 1s peaks emerged at 407.5 and 400.0 eV. These two peaks are assigned to the signal of surface adsorbed nitrates and ammonia, respectively.^[10] There is significant enhancement of the O 1s peak at 532.5 eV, which is consistent with surface nitrates. The P 2p peaks of the investigated samples remained unchanged during sonication and electrolysis. For metal cations of the first-transition series, the binding energy of 2p_{3/2} shake-up satellite peak decreases when the electronic configuration changes from d⁴ to d⁵. Thus, the 2p_{3/2} satellite peak appears at lower binding energy for Mn^{II} (d⁵). The 2p_{3/2} satellite peak of Mn^{III} (d⁴) will appear at higher binding energy, overlapping with its 2p_{1/2} peak.^[11] In addition, the energy splitting value of Mn 3s will decrease significantly from Mn^{II} to Mn^{III} because of unpaired 3d electrons in Mn^{II}.^[12] The XPS results for the above-mentioned samples clearly demonstrate the stability of the coordination environment of the Mn sites in the material when it is subjected to sonication and electrolysis.

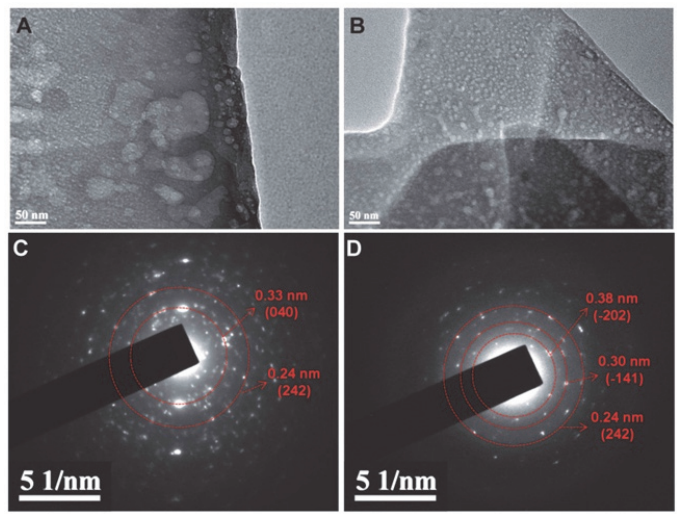
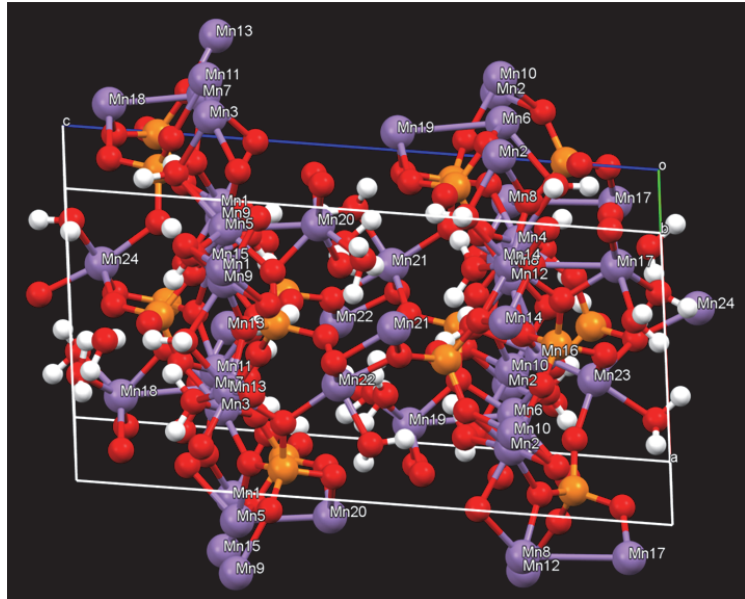


Fig. S26 The TEM images and SAED patterns of the MnPi sample before (**A, C**) and after (**B, D**) electrolysis. The holes displayed in the TEM images are caused by the electron beam.



No.	Mn site	neutral	-1e	Δ_e	No.	Mn site	neutral	-1e	Δ_e
1	Mn1	15.7	14.9	-0.8	13	Mn3	15.8	14.9	-0.9
2	Mn2	10.8	14.9	4.1	14	Mn4	15.8	14.8	-1
3	Mn1	15.7	15	-0.7	15	Mn3	15.7	14.6	-1.1
4	Mn2	15	14.8	-0.2	16	Mn4	12.4	15	2.6
5	Mn4	13.9	14.9	1	17	Mn6	14.1	14.3	0.2
6	Mn3	14	15	1	18	Mn6	17.3	14.5	-2.8
7	Mn4	12.3	15.1	2.8	19	Mn6	17.4	14.8	-2.6
8	Mn3	15.9	15	-0.9	20	Mn6	14	14.8	0.8
9	Mn2	14	14.9	0.9	21	Mn5	13.9	14.9	1
10	Mn1	15.5	14.9	-0.6	22	Mn5	15.7	14.9	-0.8
11	Mn2	14	14.9	0.9	23	Mn5	16.8	14.9	-1.9
12	Mn1	16	14.8	-1.2	24	Mn5	13.9	15	1.1

Fig. S27 (top) The unit cell of the MnPi used to calculate the order of difficulty on the oxidation of different Mn sites. The Mn sequence numbers are labeled. (bottom) The charges and charge differences of different Mn sites in the cell before and after removing one electron from the system.

Metaswitzerite $\text{Mn}_3(\text{PO}_4)_2 \cdot 4\text{H}_2\text{O}$ has a crystal structure with monoclinic symmetry. The conventional cell, being also the primitive cell, has eight chemical formula units including 200 atoms in total. The electronic configuration $[\text{Ne}]3s^23p^63d^54s^2$ is applied for the pseudopotential of Mn. Thus, the neutral Mn atom has a valence charge of $15(e^-)$, and the Mn atom with a formal oxidation state of +2 in $\text{Mn}_3(\text{PO}_4)_2 \cdot 4\text{H}_2\text{O}$ should have a valence charge of $13(e^-)$. However, the calculated atomic charges of 24 Mn atoms in the unit cell

have valence charges larger or smaller than 13(e⁻) due to the different coordination environments of Mn atoms in the lattice structure. Then, we positively charged the unit cell through reducing one electron. The decrease/increase of the atomic charges indicates the oxidation/reduction of Mn atoms. After removing one electron from the neutral unit cell, the No. 18 Mn atom has the largest reduction of atomic charge (-2.8e) among all the 24 Mn atoms, meaning that it can be oxidized most easily.

References

- [1] a) W. Jia, Z. Cao, L. Wang, J. Fu, X. Chi, W. Gao and L.-W. Wang, *Comput. Phys. Commun.*, 2013, **184**, 9-18; b) W. Jia, J. Fu, Z. Cao, L. Wang, X. Chi, W. Gao and L.-W. Wang, *J. Comput. Phys.*, 2013, **251**, 102-115.
- [2] a) D. R. Hamann, *Phys. Rev. B*, 2013, **88**, 085117; b) M. Schlipf and F. Gygi, *Comput. Phys. Commun.*, 2015, **196**, 36-44.
- [3] L. Wang and T. Maxisch, G. Ceder, *Phys. Rev. B*, 2006, **73**, 195107.
- [4] H. J. Monkhorst and J. D. Pack, *Phys. Rev. B*, 1976, **13**, 5188-5192.
- [5] L. Fanfani and P. F. Zanazzi, *Tschermaks mineralogische und petrographische Mitteilungen*, 1979, **26**, 255-269.
- [6] H.-R. Zhao, C. Xue, C.-P. Li, K.-M. Zhang, H.-B. Luo, S.-X. Liu and X.-M. Ren, *Inorg. Chem.*, 2016, **55**, 8971-8975.
- [7] O. S. Volkova, L. V. Shvanskaya, E. A. Ovchenkov, E. A. Zvereva, A. S. Volkov, D. A. Chareev, K. Molla, B. Rahaman, T. Saha-Dasgupta and A. N. Vasiliev, *Inorg. Chem.*, 2016, **55**, 10692-10700.
- [8] H.W. Nesbitt and D. Banerjee, *American Mineralogist*, 1998, **83**, 305-315.
- [9] C. Walter, P. W. Menezes, S. Orthmann, J. Schuch, P. Connor, B. Kaiser, M. Lerch and M. Driess, *Angew. Chem. Int. Ed.*, 2018, **57**, 698-702.
- [10] J. F. Moulder, W. F. Stickle, P. E. Sobol and K. D. Bomben, *Handbook of X-Ray Photoelectron Spectroscopy*, Perkin-Elmer, MN, USA, 1992.
- [11] Y. Gorlin, B. Lassalle-Kaiser, J. D. Benck, S. Gul, S. M. Webb, V. K. Yachandra, J. Yano and T. F. Jaramillo, *J. Am. Chem. Soc.*, 2013, **135**, 8525-8534.
- [12] H. Simchi, K. A. Cooley, J. Ohms, L. Huang, P. Kurz and S. E. Mohney, *Inorg. Chem.*, 2018, **57**, 785-792.